THE JOURNAL OF PHYSICAL CHEMISTRY C

Article

pubs.acs.org/JPCC

Excited States of $Pt(PF_3)_4$ and Their Role in Focused Electron Beam Nanofabrication

Matija Zlatar,[†] Michael Allan,[‡] and Juraj Fedor*[,§]

[†]Department of Chemistry, Institute of Chemistry, Technology and Metallurgy (IChTM), University of Belgrade, Njegoševa 12, P.O. Box 815, 11001 Belgrade, Serbia

[‡]Department of Chemistry, University of Fribourg, Chemin du musée 9, 1700 Fribourg, Switzerland

[§]J. Heyrovský Institute of Physical Chemistry v.v.i., The Czech Academy of Sciences, Dolejškova 3, 18223 Prague, Czech Republic

Supporting Information

ABSTRACT: Electron induced chemistry of metal-containing precursor molecules is central in focused electron beam induced deposition (FEBID). While some elementary processes leading to precursor decomposition were quantitatively characterized, data for neutral dissociation is missing. We provide this data for the model precursor $Pt(PF_3)_4$ by using the available cross sections for electronic excitation and characterizing fragmentation of the excited states theoretically by TDDFT. The potential energy curves for a number of states visible in the experimental electron energy loss spectra are dissociative, either directly or via conical intersections, indicating that the quantum yield for dissociation is close to 100%. Taking into account typical electron energy distribution at the FEBID spot reveals that the importance of neutral dissociation exceeds that of dissociative electron attachment, which has been so far considered to be the dominant decomposition process. We thus established neutral dissociation as an important, albeit often neglected, channel for FEBID using $Pt(PF_3)_4$. The calculations revealed a number of other phenomena that can play a role in electron induced chemistry of this compound, e.g., a considerable increase of bond dissociation energy with sequential removal of multiple ligands.

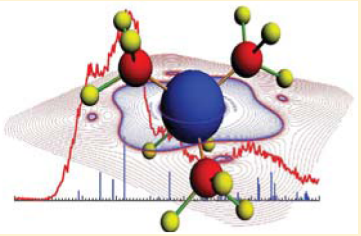

INTRODUCTION

Focused electron beam induced deposition (FEBID) is a method for producing 3D metallic structures of sub-10 nm dimensions on planar or even nonplanar surfaces.[1] The often metal-containing precursor molecules are physisorbed on a substrate and exposed to focused high-energy (keV) electron beam which degrades them to yield a metal deposit. The challenges of the technique are to increase the metal content of the deposits which is often less than 50%, yielding a conductivity far below that of bulk metal and improving deposit widths which are usually a multiple of the electron beam diameter.[2] An important prerequisite for resolving the above-mentioned problems is the understanding of the fundamental gas phase electron-driven chemistry of the volatile metal complexes used as precursors.

Four classes of processes contribute to the electron-driven degradation of the precursors[3]

$$
\begin{aligned}
e^- + AB \rightarrow [AB]^- &\rightarrow A + B^- && \text{DEA}\\
&\rightarrow AB^* + e^- \rightarrow A + B + e^- && \text{ND}\\
&\rightarrow AB^+ + 2e^- \rightarrow A + B^+ + 2e^- && \text{DI}\\
&\rightarrow AB^{**} + e^- \rightarrow A^- + B^+ + e^- && \text{BD}
\end{aligned}
$$

where DEA stands for dissociative electron attachment, generally mediated by a transient anion AB^-, ND stands for neutral dissociation, generally mediated by an electronically excited state of the precursor AB*, DI stands for dissociative ionization, and BD stands for bipolar dissociation. Their thorough knowledge would, ideally, permit designing precursors where the processes yielding the desired deposit properties dominate. Two elementary processes have been studied more thoroughly: DEA[4−7] and DI.[7,8] In contrast, the study of ND process has been almost completely neglected, in part for technical reasons—it is much easier to mass spectrometrically detect the charged products of DEA or DI than the neutral products of ND.

The aim of this work is to provide an indication of how important is the ND channel in the model precursor $Pt(PF_3)_4$, tetrakis(trifluorophosphine)platinum(0). We rely on the fact that the first step, the electronic excitation by electron impact, has been measured quantitatively[9] and predict the dissociative behavior of the excited states with a theoretical study of the potential energy surfaces of the excited states. We have chosen the precursor $Pt(PF_3)_4$ for our study because it is promising from the point of application since it is carbon-free and thus avoids the otherwise notorious carbon residues in the deposits and because the electron-driven processes in the gas phase have been thoroughly studied. In particular, the electronic excitation by electron impact[9] and the dissociative electron attachment[5] have both been studied quantitatively; i.e., absolute cross sections for these processes have been measured. The electron-induced chemistry has been also probed for this precursor adsorbed on the surfaces.[10]

From a computational point of view, calculations of the electronic structure of $Pt(PF_3)_4$ present a number of challenges

Received: March 14, 2016
Revised: April 22, 2016
Published: April 25, 2016

DOI: 10.1021/acs.jpcc.6b02660
J. Phys. Chem. C 2016, 120, 10667−10674

related to a large number of electrons, in particular, relativistic electrons in the inner shells. The complications are augmented for the calculations of excited states and even more for the calculations of the potential energy surfaces required to assess the dissociative behavior. We have utilized the density functional theory (DFT) and time-dependent density functional theory (TDDFT) based approaches, and it was necessary to employ different exchange-correlation approximations suited for a given type of calculation.

METHODS

All calculations were done using the DFT and TDDFT approaches as implemented in the ADF program package,[11,12] with an all electron triple-ζ Slater-type orbitals plus one polarization function (TZP) basis set, and Becke's integration grid of good quality.[13,14] In order to account for relativistic effects, we used the zeroth-order regular approximation to the Dirac Hamiltonian in the scalar-relativistic formulation (SR-ZORA).[15] Geometry optimization was performed using the local density approximation (LDA) characterized by the Vosko−Willk−Nusair parametrization (VWN5),[16] constraining the symmetry of $Pt(PF_3)_4$ to T_d point group. In addition, hybrid Becke 3-parameter with 20% of Hartree−Fock (exchange), VWN5 Lee−Yang−Parr (correlation), i.e. B3LYP[17] functional, and B3LYP with Grimme's third-generation dispersion energy correction[18] and Becke−Johnson dumping,[19] i.e., B3LYP-D3 functional, were used.

Heterolytic Pt−(PF_3) bond dissociation energy (BDE) was calculated as the difference between the energy of the complex and the sum of the energies of the isolated, optimized fragments. Harmonic frequencies were calculated at the corresponding level of theory in order to ascertain that the optimized structures correspond to the minima on the potential energy surface and to evaluate the zero-point energy effects.

The nature of metal−ligand bonding in $Pt(PF_3)_4$ was analyzed with the aid of the extended transition state (ETS) energy decomposition scheme[20] as implemented in ADF.[11] The interaction energy between $Pt(PF_3)_3$ and PF_3 fragments is decomposed into four components: $E_{int} = E_{elst} + E_{Pauli} + E_{orb} + E_{disp}$. E_{elst} is the classical electrostatic interaction between the fragments; E_{Pauli} is the repulsive Pauli interaction between occupied orbitals on the two fragments; E_{orb} is the stabilizing interaction between the occupied MOs from one fragment with the unoccupied MOs of the other fragment and polarization in the same fragment; E_{disp} is the dispersion part of the interaction energy, E_{int}. In addition to the E_{int}, the preparation energy E_{prep}, the energy required to bring separated $Pt(PF_3)_3$ and PF_3 fragments from their equilibrium geometry to the geometry they adopt in $Pt(PF_3)_4$, is considered to get BDE, $-BDE = E_{int} + E_{prep}$. Additionally, a decomposition of the electron density deformation on the basis of the orbitals of each isolated fragment via natural orbitals for chemical valence (NOCV)[21] was performed in order to elucidate different density transfer channels and to quantify their importance, either by the amount of charge transferred or as an energy contribution of each deformation density route to the E_{orb}.

BDE for consecutive elimination of PF_3 ligands has been calculated, and ETS-NOCV analysis has been performed in an analogous way. Ground states of all investigated complexes are taken to be singlets, while for the calculation of atomic states of free Pt atom, both closed shell $5d^{10}$ and open shell $5d^96s^1$ configurations are considered, the latter one in an unrestricted formalism.

Dissociation of the PF_3 ligand was studied via relaxed linear transit scan, changing Pt−P distance from 2.0 to 10.0 Å in 50 steps. During the scan, symmetry was kept to the C_{3v} point group. Potential energy curves of the excited states of $Pt(PF_3)_4$ were evaluated by adding the excitation energies, calculated by TDDFT, to the ground state energies.

The LDA functional yielded ground-state geometry and frequencies with the best agreement with the available experimental data. Therefore, this geometry has been used for calculating the vertical excitation energies in T_d symmetry with the SAOP functional,[22] a special functional designed for the calculations of response properties—an essential point when addressing positions of high-lying states.[23] This level of theory failed in describing the situation far from the minimum, i.e., for calculating potential energy curves for dissociation of a ligand. First, LDA is known to show overbinding effects.[24] It should be pointed out that B3LYP shows an opposite trend, weakening metal−ligand bond,[25] and thus neither LDA nor B3LYP describes energetics of the ground state properly. However, adding dispersion correction makes B3LYP more accurate.[26] The C_{3v} symmetry-constrained relaxed ground-state potential curve was therefore calculated with the hybrid dispersion-corrected B3LYP-D3 functional. The second problem at long Pt−P distances appeared when considering excitation energies with the SAOP functional. For example, at a Pt−P distance of 10 Å, where the PF_3 ligand is essentially dissociated, the lowest excited states should correspond to those of $Pt(PF_3)_3$. Unfortunately, at long Pt−P distances a number of nonphysical charge-transfer states (from $Pt(PF_3)_3$ to PF_3) are present when SR-SAOP/TZP level of theory is used; thus, some of the potential energy curves do not exhibit the correct asymptotic behavior. In order to deal with these intermolecular charge transfer states, the "half-and-half" functional, with 50% of Hartree−Fock exchange, BHandHLYP, was used to explore the potential energy surfaces of excited states as suggested in the literature.[27,28] With this method, the asymptotic limits of excited states shown now exactly match the excited states of $Pt(PF_3)_3$. For other states, both SAOP and BHandHLYP show qualitatively the same results.

RESULTS AND DISCUSSION

Ground State. We have first tested the performance of different methods on the experimentally known characteristics of $Pt(PF_3)_4$. The tables comparing the presently calculated Pt−P bond length and vibrational frequencies with experimental data[29−31] and with previous calculations[29,32] are provided in the Supporting Information. The best agreement has been achieved with the LDA functional, geometry, and vibrational frequencies agreeing in all cases to better than 5%. The hybrid B3LYP and dispersion-corrected B3LYP-D3 functionals yield similar results except for a slightly longer ground state Pt−P bond lengths. We have also performed calculations without relativistic corrections to test their importance. The agreement of the nonrelativistic calculations with experimental data is considerably worse in all cases.

The dispersion and zero point energy corrected bond energy with included relativistic effects is 0.85 eV (SR-B3LYP-D3/TZP). This value is in agreement with previously reported BDE of 0.97 and 1.08 eV at the BP86 and mPW91PW91 level of theory,[32] respectively. The inclusion of the dispersion correction to the B3LYP functional is essential for the calculation of Pt-(PF_3) BDE. Taking the dispersion into account increases the bond dissociation energy almost by a

DOI: 10.1021/acs.jpcc.6b02660
J. Phys. Chem. C 2016, 120, 10667−10674

Table 1. ETS-NOCV Energy Decomposition Analysis of $Pt(PF_3)_3-PF_3$, $Pt(PF_3)_2-PF_3$, $Pt(PF_3)-PF_3$, and $Pt-PF_3$[a]

	$Pt(PF_3)_3-PF_3$	$Pt(PF_3)_2-PF_3$	$Pt(PF_3)-PF_3$	$Pt-PF_3$
Pt−P length	2.266	2.242	2.207	2.064
E_{Pauli}	7.72	7.69	7.01	13.54
E_{elst}	−6.05	−6.15	−5.87	−11.52
E_{disp}	−0.36	−0.26	−0.18	−0.15
E_{orb}	−2.92	−2.93	−2.90	−5.21
E_{orb}^{σ} (Δq)	−1.15 (0.52)	−1.09 (0.48)	−1.18 (0.49)	−1.97 (0.90)
$E_{orb}^{\pi*}$ (Δq)	−1.20 (0.70)	−1.31 (0.75)	−1.35 (0.72)	−2.38 (0.88)
$E_{orb}^{\sigma*}$ (Δq)	−0.48 (0.21)	−0.46 (0.21)	−0.32 (0.17)	−0.79 (0.28)
E_{int}	−1.60	−1.64	−1.94	−3.33
E_{prep}	0.70	0.49	0.45	0.53
BDE	0.91	1.15	1.49	2.81
BDE + ΔZPE	0.85	0.97	1.65	2.74

[a]Energy components are given in eV; Pt−P bond lengths in Å. Orbital contribution is decomposed to the contributions of σ-donation, π*-back-donation, and σ*-back-donation; the charge transfer through these channels, Δq, is indicated in parentheses.

factor of 2. The addition of zero point energy slightly lowers the BDE; it is a correction that favors dissociation. Relevance of the included dispersion for the calculation of BDE with the B3LYP functional is important for the analogue complex of Ni(0). BDE of $Ni(PF_3)_4$, calculated at the SR-B3LYP-D3/TZP level of theory, with zero point energy is 1.26 eV, comparing to the BDE of 0.87 eV without dispersion and to the previously communicated BDE of 0.94 eV at the B3LYP/6-311+G(3df) level of theory.[33]

We have also calculated BDE for sequential removal of PF_3 ligands, i.e., formation of $Pt(PF_3)_2$, $Pt(PF_3)$, and Pt(0), summarized in Table 1. BDEs for removal of the second, third, and fourth ligand at the SR-B3LYP-D3/TZP level of theory with zero point corrections are 1.09, 1.65, and 2.74 eV, respectively. The PF_3 dissociation energies thus increase with decreasing numbers of PF_3 groups. The total energy needed for removal of four ligands is 6.33 eV and average $Pt-PF_3$ BDE is 1.58 eV. The increase of the binding energy with ligand removal is much stronger than in other FEBIP precursors, e.g., in $Fe(CO)_5$.[34] Dissociation of the last PF_3 ligand comprises the changing of the spin state of the system. Electronic configuration of Pt changes from closed shell $5d^{10}$ in complexes to the ^3D ground state term ($5d^96s^1$ electronic configuration) of the free atom. The energy difference between the two configurations at SR-B3LYP/TZP level of theory is 0.50 eV, in accordance with other DFT estimates.[35] Inclusion of spin−orbit coupling (SOC) in ZORA formalism leads to the energy difference of 0.69 eV, in agreement with the experimental value of 0.76 eV.[36]

Nature of Pt−P Bond. Before discussing the electron excitations in $Pt(PF_3)_4$, it is important to understand the low Pt−P binding energy and consequently the bonding situation in the ground state of the complex. A qualitative MO diagram for $Pt(PF_3)_4$ illustrating the most important orbital interactions between PF_3 MOs and Pt orbitals is shown in Figure 1. $Pt(PF_3)_4$ is a tetrahedral d^{10} complex of Pt(0). Five 5d orbitals of Pt atom split into two levels, 9e and $22t_2$. Lower lying 9e MOs are clearly nonbonding $d_{x^2-y^2}$ and d_{z^2} orbitals on Pt. $22t_2$ MOs result from antibonding overlap of Pt 5d orbitals and PF_3 σ lone pairs and, additionally, from bonding interactions between Pt 5d orbitals and empty σ* P−F orbitals. The latter interaction is the most important for stabilizing the $22t_2$ MO's. This back-donation is crucial for the coordination chemistry of complexes with phosphine type ligands.[37,38] Detailed compositions of these MOs as well as of lowest unoccupied MO's of $Pt(PF_3)_4$ are given in Figure 1.

To provide the quantitative information about the bonding, ETS-NOCV energy decomposition analysis has been performed, and the results are summarized in Table 1. The results for the species that emerge from sequential removal of PF_3 ligands are given for comparison as well, while the results for $Pt(PF_3)_3-PF_3$ at different levels of theories are given in the Supporting Information.

The nature of Pt−P bonding can be understood from the examination of the attractive interactions. E_{elst} and E_{orb} are the indication of ionic vs covalent bonding, respectively. Thus, the Pt−P bond can be understood as 65% ionic and 31% covalent, while the dispersion contributes by 4%. As a consequence of the high ionic character of the Pt−P bond, dissociation of a PF_3 ligand is heterolytic.

In order to get the BDE, it is necessary to add E_{prep} to the interaction energy. E_{prep} is mainly given by the deformation energy of $Pt(PF_3)_3$ because of a large change in the geometry-relaxed $Pt(PF_3)_3$ is in trigonal-planar coordination while it adopts pseudotetrahedral geometry in $Pt(PF_3)_4$. Changes in the geometry of the PF_3 ligand are negligible. Differential zero-point energy, ΔZPE, as already mentioned, somewhat lowers BDE.

Higher BDE for the dissociation of the second PF_3 is mainly due to the lower E_{prep} (Table 1), that is because of the smaller changes in the geometry of $Pt(PF_3)_2$. In the case of removal of the third PF_3, BDE is even higher, primarily because of the changes in E_{Pauli} and E_{elst}, their sum being less destabilizing than in the previous two cases. Finally, in the case of the elimination of the fourth ligand, E_{Pauli}, E_{elst}, and E_{orb} have significantly higher values because of the shortest Pt−P distance, 0.2 Å shorter than in $Pt(PF_3)_4$. Change of BDE in this case is essentially due to the increase of covalent bonding because of the larger change in E_{orb} than in the sum of E_{Pauli} and E_{elst}.

NOCV scheme reveals four dominant electron density flow channels during the bond formation. Illustration of these deformation density contributions is given in Figure 2, where red color represents electron outflow and blue electron inflow. The first contribution is the σ-donation from the lone pair of phosphorus atoms and the charge accumulation in the bonding region. The next two contributions (degenerate ones) indicate the π*-back-donation from Pt d orbitals. The last contribution is the σ*-back-donation. A quantitative measure of the σ/π donor/acceptor abilities of PF_3 ligand, either as the total charge

DOI: 10.1021/acs.jpcc.6b02660
J. Phys. Chem. C 2016, 120, 10667−10674

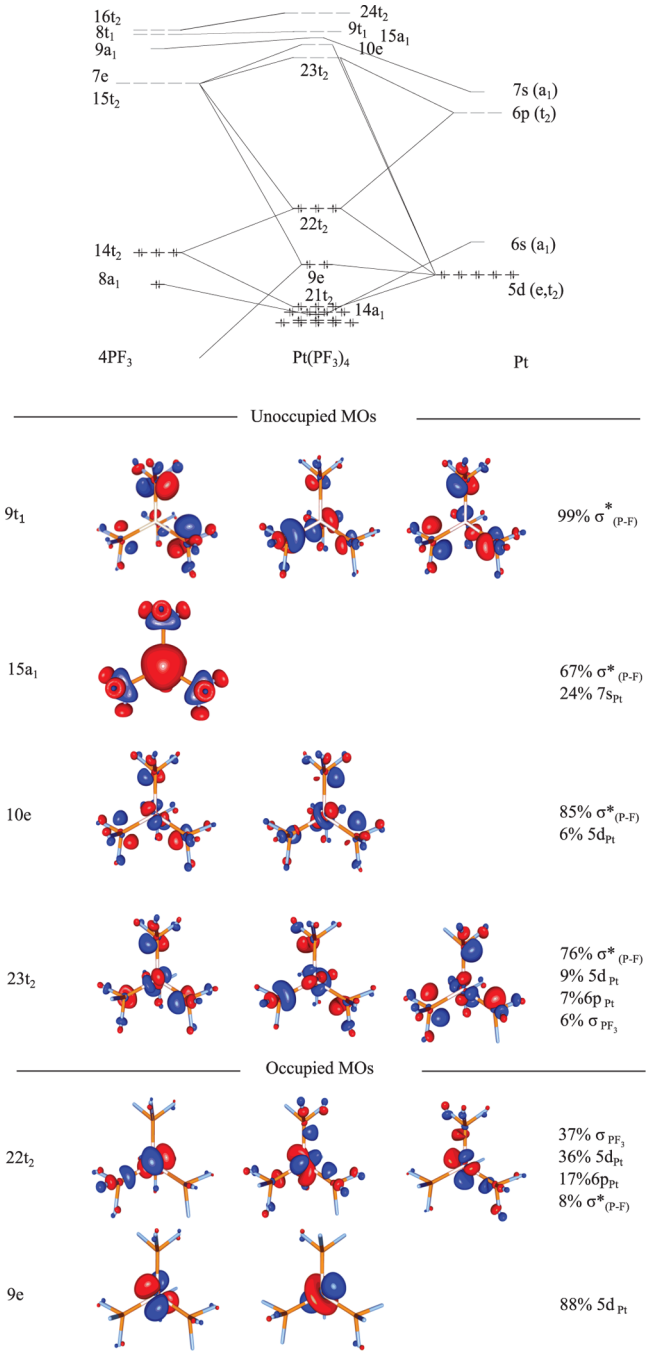

Figure 1. Qualitative molecular orbital diagram for $Pt(PF_3)_4$ (based on SR-B3LYP-D3/TZP) together with their occupation in the ground state and graphical representation of individual MO's (isovalue 0.07 au). Composition of each MO is given as well.

transferred trough these channels or as the energy contributions to the E_{orb} (Table 1), indicates that the back-donation from the filled Pt d orbitals into the σ^* P−F orbitals of PF_3 is a dominant bonding pathway. Linking these results to the MO scheme in $Pt(PF_3)_4$ undoubtedly reveals the significance of $22t_2$ MO in the formation of the Pt−P bond.

Excited States. Figure 3 compares the present theoretical transition energies and, in the case of allowed transitions, the calculated oscillator strengths, with electron energy loss spectra of $Pt(PF_3)_4$ recorded under conditions where either dipole-allowed transitions (top curve, θ = 0°, E_r = 30 eV) or spin-forbidden transitions (bottom curve, θ = 180°, E_r = 0.5 eV) are enhanced.[39] The calculated transition energies, oscillator strengths, state symmetries, and compositions of states in terms of linear combinations of single excitations are given in the Supporting Information.

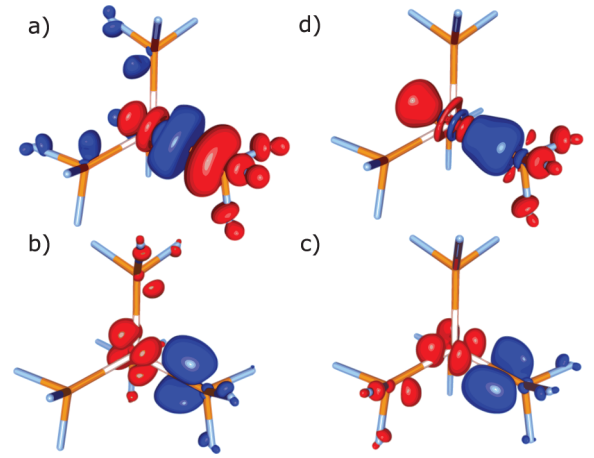

Figure 2. Most important deformation density channels during the $Pt(PF_3)_3$−PF_3 bond formation from ETS-NOCV analysis. Their relevance is given by the total charge transferred, Δq, and by energy contribution E^i_{orb} to the E_{orb}: (a) σ-donation (Δq = 0.52, E^σ_{orb} = −1.15 eV; isovalue 0.003 au); (b) and (c) π-back-donation (Δq = 0.70, E^π_{orb} = −1.20 eV; isovalue 0.003 au); (d) σ-back-donation (Δq = 0.21, $E^{\sigma*}_{orb}$ = −0.47 eV; isovalue 0.001 au). Red/blue color represent electron outflow/inflow.

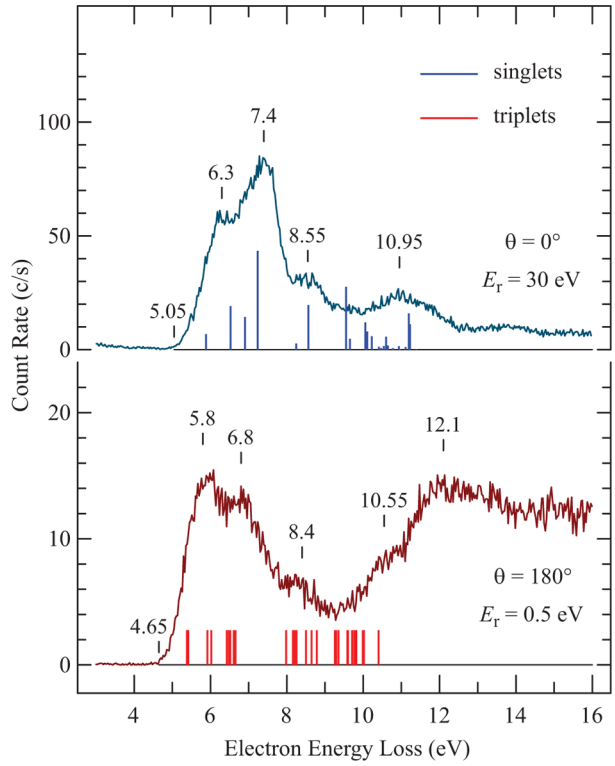

Figure 3. Comparison of the present calculated transition energies, shown by vertical lines, with electron energy loss spectra[9] enhancing either dipole-allowed spin-conserving transitions (top curve, θ = 0°, E_r = 30 eV) or spin-forbidden transitions (bottom curve, θ = 180°, E_r = 0.5 eV). Heights of the lines under the singlet spectrum indicate oscillator strengths.

DOI: 10.1021/acs.jpcc.6b02660
J. Phys. Chem. C 2016, 120, 10667−10674

$Pt(PF_3)_4$ has the T_d symmetry in its ground state energy minimum, and the excited states span the A_1, A_2, E, T_1, and T_2 irreducible representations of this point group. Owing to its high symmetry, there is a large number of multiplets arising from single excitations between occupied and unoccupied MOs of $Pt(PF_3)_4$. State symmetries are determined from the direct product of irreducible representations that filled and empty MO belong to. For example, the HOMO → LUMO transition, $22t_2 \rightarrow 23t_2$, will give rise to a set of singlet and triplet states belonging to irreducible representations appearing in the $T_2 \otimes T_2 \subset A_1 + E + T_1 + T_2$. Only transitions to the $^1T_2$ states are spin- and dipole-allowed and are shown in the top panel of Figure 3.

The calculated bar spectra in Figure 3 are in an excellent agreement with the experiment for both the singlet and the triplet excited states. The calculation satisfactorily reproduces the small singlet−triplet splitting. Figure 3 indicates an observed difference between the onset energies of the singlet and triplet spectra of only 0.4 eV. The calculated singlet−triplet differences for the lowest excited states are 0.33 eV when the lowest dipole forbidden transition is taken and 0.50 eV when the lowest dipole-allowed transition is taken. The energy difference between singlets and triplets arising from the same orbital excitation depends on the overlap between the MOs with unpaired electrons. Lowest excited states are the result of the promotion of an electron from HOMO ($22t_2$) that is localized on Pt−P bond to the empty orbitals that are spread over ligands (Figure 1). Therefore, the small singlet−triplet separation is a consequence of a small spatial overlap between related MOs, resulting in a small exchange integral. Singlet−triplet splitting of metal-to-ligand charge transfer transitions in organometallic compounds is of order 0.2−0.5 eV,[40−42] as found here for $Pt(PF_3)_4$.

For singlet states, the oscillator strengths reflect all the experimental features: the slow gradual rise of the signal in the 5.2−6 eV range, bands observed at 6.3, 7.4, and 8.55 eV, and the broad band peaking at 10.95 eV. The oscillator strength of the transition calculated at 9.55 eV appears to be too large, but there is clear evidence for this transition in the experimental spectrum. Very good agreement is obtained also for the triplet states: the bands at 5.8, 6.8, and 8.4 eV have exact counterparts in calculated states. Transitions, both singlet and triplet, calculated up to around 8.2 eV are due to the excitations from $22t_2$ MO.

The indispensability of the relativistic correction is revealed by spectra calculated with a nonrelativistic model and presented in the Supporting Information. We have calculated the excitation spectrum also for spin−orbit mixed states with ZORA spin−orbit formalism at the same level of theory (Figure S1 in Supporting Information), and the spectrum looks very similar to the one shown in the upper panel of Figure 3. This implies that effect of SOC is small. The consequences of SOC are twofold: splitting of originally triplet states and singlet−triplet mixing, the latter, in principle, important for the intensity of the dipole-allowed transitions. Spin−orbit states are characterized by their T_d^* double-group irreducible representations and parentage in terms of contributing singlet and triplet states. The spin−orbit states of T_2 double-group symmetry are dipole-allowed. Triplet states split according to the direct product of the spin symmetry (T_1 for triplets) and orbital symmetry. Therefore, after SOC is included, $^3A_1$ states become T_1, $^3A_2$ become T_2, ^3E split into $T_1 + T_2$, $^3T_1$ into $A_1 + E + T_1 + T_2$ while $^3T_2$ into $A_2 + E + T_1 + T_2$. Considering, for example, spin flip $22t_2 \rightarrow 23t_2$, four spin-free triplets split with SOC into 11 spin−orbit states that lie in a narrow energy range <0.2 eV. Singlet states obviously do not split because the spin singlets are totally symmetric. Singlet−triplet mixing, as it can be seen when comparing the calculated spectra with and without SOC Figure 3, is also small. Therefore, the classical picture of pure spin states (singlets and triplets) remains even after inclusion of SOC. This may seem surprising because SOC constant of Pt 5d orbitals is large, approximately 0.5 eV.[43] However, this is SOC constant of free Pt atom, not when Pt is in a complex, where SOC is quenched by coordinated ligands. In fact, poor SOC in $Pt(PF_3)_4$ is due to the modest participation of Pt 5d orbitals in orbitals involved in transitions, Figure 1. Small spin−orbit interactions are present in other tetrahedral d^{10} organometallic compounds.[40,44,45] In the following we thus, for the sake of simplicity, present potential energy surfaces of noncoupled states.

Potential Surfaces. The potential energy curves for the ground and excited states (up to 8.5 eV) are shown in Figure 4.

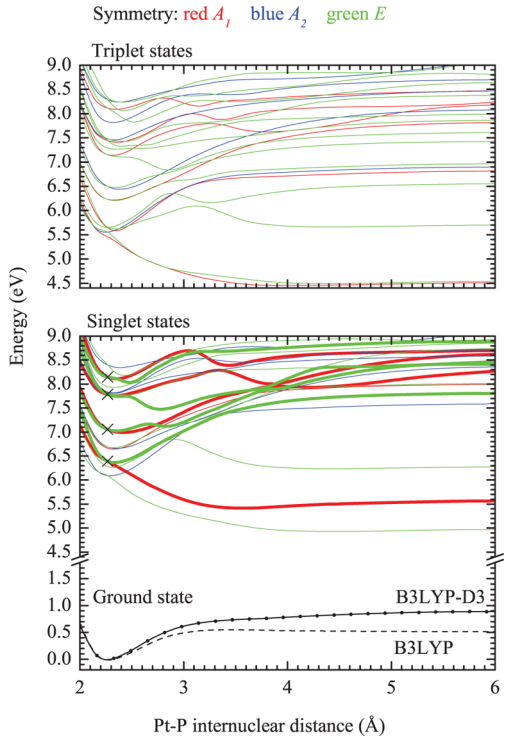

Figure 4. Relaxed C_{3v} symmetry constrained potential energy scans of the ground and excited states. All states up to 8.5 eV excitation energy (at equilibrium ground state geometry) are shown and are colored according to their symmetry. Crosses correspond to the first four vertical dipole-allowed transitions (in T_d symmetry) visible in the top panel of Figure 3 and the potential curves of the $^1A_1$ and ^1E states corresponding to these transitions are shown in bold. The energies were calculated at the points shown on the ground state curve for all curves, but only splines are shown for the excited states. The different position of crosses when compared to transitions in Figure 3 is explained in the text.

Importance of the dispersion correction, discussed above, is illustrated by the potential energy curves calculated with and without the dispersion correction shown at the bottom of Figure 3. Because of the reasons described in the Methods section, excited states were calculated at different level of theory than the spectra shown in Figure 3, the energies are thus shifted

DOI: 10.1021/acs.jpcc.6b02660
J. Phys. Chem. C 2016, 120, 10667−10674

by approximately 0.5 eV. The lowest four are marked with a cross in Figure 4. Our potential curves refer to dissociation of one ligand in a symmetry lowered to C_{3v}. Because of this symmetry descent, orbitally triple degenerate states split into two components, $T_2 \rightarrow A_1 + E$ and $T_1 \rightarrow A_2 + E$ in the C_{3v} point group, as can be clearly seen in Figure 4. In the C_{3v} symmetry, transitions to the A_1 and E states are dipole-allowed. The energies and assignments of the individual states can be found in the Supporting Information.

From the shape of the potential energy curves it is possible to predict whether the excited molecule will expel one of its ligands. The lowest dipole-allowed state is directly dissociative in its A_1 component, resulting in the loss of one PF_3 ligand. The second dipole-allowed state is bound in the adiabatic representation, but the E component clearly shows avoided crossings with several states of the same symmetry. The excited complex will thus dissociate via conical intersections which will develop when the C_{3v} constraint is relaxed. The same is valid for the third and fourth dipole-allowed transitions: even though the adiabatic curves are bound, their shape shows a number of avoided crossings which will become conical intersections and thus show dissociative behavior upon breaking the C_{3v} symmetry. It is also worth noticing that both the lowest singlet and triplet states are directly dissociative. This is relevant because electron impact also induces spin-forbidden transitions as shown in the lower panel of Figure 3. At long Pt−P bond distances, the excited states shown on Figure 4 are those of $Pt(PF_3)_4$ because of the heterolytic nature of the dissociation and because there is no change in the spin ground state during a course of dissociation.

Qualitatively speaking, loss of PF_3 upon excitation can be understood from the analysis of the nature of the Pt−P bond presented in the previous section. As already mentioned, the lowest excited states of $Pt(PF_3)_4$ are results from the promotion of an electron from $22t_2$ MO (Figure 1). This MO is crucial for the back-donation, which in turn is the main orbital contribution for the strength of the Pt−P bond. Therefore, one electron less in this MO will weaken the Pt−P bond. At the same time, placement of this electron to an essentially metal−ligand antibonding MO, $23t_2$, will lead directly to the loss of PF_3. The two lowest singlet and two lowest triplet states, $^{1,3}T_1$ and $^{1,3}T_2$, the four excited states that are directly dissociative, are exactly the states corresponding to the $22t_2 \rightarrow 23t_2$ promotion. In addition, this excitation will produce nontotally symmetric distribution of the electrons in both of these triply degenerate orbitals. Accordingly, these electronic states will be subject to strong vibronic coupling—the Jahn−Teller (JT) effect.[46] This coupling between vibrational motion and degenerate electronic states breaks the degeneracy of the states and lowers the energy of one of its components. It should be noted that the symmetry of the ground state minimum, T_d, and symmetry of the excited states under consideration, T_1 or T_2, dictate that the JT active distortion belongs to the T_2 irreducible representation, which is the symmetry of the asymmetric Pt−P stretch. Initial Pt−P elongation, close to the ground state minimum, is primarily described by the asymmetric Pt−P stretch. Therefore, the JT effect in these excited states induces the loss of one ligand. It should be pointed out that large distortions of the lowest excited states are common feature of d^{10} tetrahedral organometallic compounds that is detected by the large Stokes shift in the fluorescence spectra.[40,44]

Implications for FEBID. The above section has shown that a majority of the low-lying electronically excited states are dissociative with respect to the loss of a PF_3 ligand. For the following we shall therefore assume that the cross section for neutral dissociation is equal to the cross section for electronic excitation. To assess the importance of neutral dissociation in FEBID and to compare it to the role of DEA, one has to consider the cross sections for the two processes and how they overlap with the energy distribution of the electrons in the FEBID reaction spot.

These questions are addressed in Figure 5. The incoming electrons in the electron beam have keV energies, but a considerable part of the chemistry is induced by the much larger number of slow secondary electrons. Their typical distribution[47] is shown by the dashed line in Figure 5. The DEA cross section is with 2 Å^2 very high in $Pt(PF_3)_4$,[5] but the band is narrow and situated at low energy where the secondary electron density is quite low. The quantity required to determine the importance of electronic excitation is the integral cross section, obtained by integrating the experimentally determined angle-resolved (differential) cross section over all possible angles of scattered electrons. The differential cross section for dipole-allowed transitions is strongly forward peaked and attains very high values in the forward direction as shown in the top panel of Figure 5. Integration including larger angles where the differential cross section is smaller reduces the value, but the result is still substantial. The integral cross section for exciting all excited states up to 9 eV,[9] indicated by the red circles in the lower part of Figure 5, is higher than the cross section for DEA. Moreover, it extends over a wider energy range so that the overlap with the energy distribution is much larger. If we

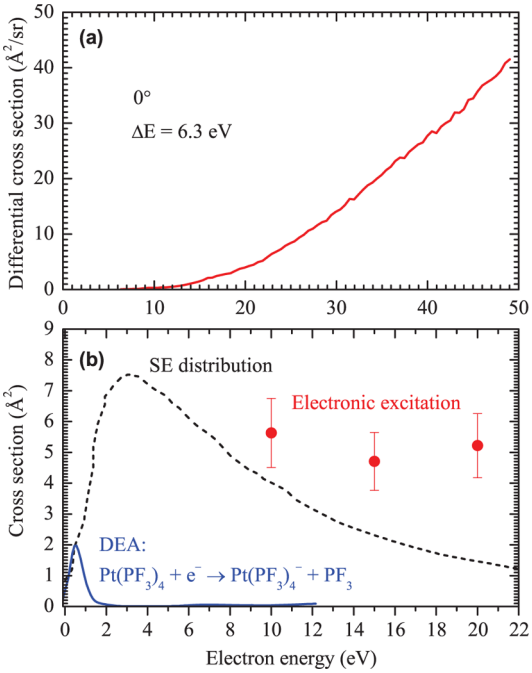

Figure 5. Comparison of integral cross sections for electronic excitation with those of the DEA channel. Bottom panel: the absolute DEA cross section[5] is shown by the solid blue line. Integral absolute cross sections for exciting all electronic states up to 9 eV[9] are shown as red circles. Representative energy distribution of secondary electrons[47] is shown by dashed line. Top panel: differential (angle resolved) cross section for exciting the state at 6.3 eV in the forward direction.

DOI: 10.1021/acs.jpcc.6b02660
J. Phys. Chem. C 2016, 120, 10667−10674

approximate the shape of electronic excitation cross section by a step-function which is zero below 6 eV and 5 Å^2 above, the overlap integral between the cross section and secondary electron distribution has a value 55 times larger for electronic excitation than for DEA. This estimate indicates the relative importance of the two processes at typical FEBIP conditions.

Two factors can change this ratio, each in a different way. Since the differential cross section (Figure 5a) is rising with electron energy, it is probable that the integral cross section will rise as well (in the above estimate it was assumed to be constant) which will raise its importance even further. On the other hand, the experimental secondary electron distribution does not include electrons that are trapped at the surface in image-potential states with energies typically up to 0.5 eV.[48] Wave functions of these electrons can have spatial extent exceeding 10 Å, from the surface,[49] and they may thus lead to DEA and increase its importance. Their abundance under FEBID conditions is unfortunately difficult to quantify.

It should also not be overlooked that DEA can be caused only by the secondary electrons (shown in Figure 5a), while electronic excitation can be caused also by the primary high-energy beam (keV), or the so-called backscattered electrons with intermediate energies (>50 eV). Even though it is commonly stated that the secondary electrons dominate the chemical changes (due to their large number resulting from avalanche processes), in some cases the primary electrons were shown to dominate the precursor decomposition process.[50,51] This further enhances the importance of the present findings.

CONCLUSIONS

We have theoretically characterized ground and excited states for the model FEBID precursor $Pt(PF_3)_4$. Present findings have a number of implications in the electron-induced chemistry of this complex. The metal−ligand bond which is rather weak in the intact complex (BDE = 0.85 eV) gets stronger with sequential removal of multiple ligands (1.09, 1.65, and 2.74 eV for removal of second, third, and fourth ligand). This increase may contribute to the fact that upon the decomposition of surface-adsorbed $Pt(PF_3)_4$ upon electron irradiation initially proceeds through single $Pt-PF_3$ bond cleavage.[10]

The calculated electronically excited states (up to 13 eV) were validated by the comparison with electron energy loss spectra. Calculation of potential energy curves has then shown that the lowest excited states are either directly dissociative along the $Pt-PF_3$ distance or undergo a number of conical intersections which will open the dissociation pathways. This indicates that the neutral dissociation path must have a cross section comparable to that for electronic excitation. Taking the overlap of the cross sections with a typical secondary electron distribution at the FEBID spot then revealed that the total importance of neutral dissociation exceeds that of DEA in $Pt(PF_3)_4$, despite the fact that $Pt(PF_3)_4$ has an unusually large DEA cross section in the gas phase. We thus established neutral dissociation as an important, albeit largely neglected, channel for FEBID using $Pt(PF_3)_4$ as a precursor. This conclusion is likely to apply to other precursors as well.

ASSOCIATED CONTENT

Supporting Information

The Supporting Information is available free of charge on the ACS Publications website at DOI: 10.1021/acs.jpcc.6b02660.

(1) Test of the performance of theoretical methods on the known properties of $Pt(PF_3)_4$; (2) bonding analysis; (3) tables containing energies, oscillator strengths, and compositions of the excited states shown in Figures 3 and 4 (PDF)

AUTHOR INFORMATION

Corresponding Author

*E-mail juraj.fedor@jh-inst.cas.cz; phone +420 266053206 (J.F.).

Notes

The authors declare no competing financial interest.

ACKNOWLEDGMENTS

This work has been supported by the Serbian Ministry of Science under project 172035 and by the Swiss National Science Foundation, project No. 200020-144367/1. J.F. acknowledges support from the COST action CM1301 CELINA.

REFERENCES

(1) Utke, I.; Gölzhäuser, A. Small, Minimally Invasive, Direct: Electrons Induce Local Reactions of Adsorbed Functional Molecules on the Nanoscale. *Angew. Chem., Int. Ed.* **2010**, *49*, 9328−9330.

(2) Utke, I.; Hoffmann, P.; Melngailis, J. Gas-assisted Focused Electron Beam and Ion Beam Processing and Fabrication. *J. Vac. Sci. Technol. B* **2008**, *26*, 1197−1276.

(3) Moore, J. H.; Swiderek, P.; Matejčík, Š.; Allan, M. In *Fundamentals of Interactions of Electrons with Molecules in Nano-fabrication Using Focused Ion and Electron Beams: Principles and Applications*; Utke, I., Moshkalev, S., Russel, P., Eds.; Oxford University Press: 2012; pp 184−225.

(4) Engmann, S.; Stano, M.; Matejčík, Š.; Ingólfsson, O. The Role of Dissociative Electron Attachment in Focused Electron Beam Induced Processing: A Case Study on Cobalt Tricarbonyl Nitrosyl. *Angew. Chem., Int. Ed.* **2011**, *50*, 9475−9477.

(5) May, O.; Kubala, D.; Allan, M. Dissociative Electron Attachment to $Pt(PF_3)_4$ - a Precursor for Focused Electron Beam Induced Processing. *Phys. Chem. Chem. Phys.* **2012**, *14*, 2979−2982.

(6) Engmann, S.; Omarsson, B.; Lacko, M.; Stano, M.; Matejčík, Š.; Ingólfsson, O. Dissociative Electron Attachment to Hexafluoroacetylacetone and its Bidentate Metal Complexes M(hfac)(2); M = Cu, Pd. *J. Chem. Phys.* **2013**, *138*, 234309.

(7) Engmann, S.; Stano, M.; Matejčík, Š.; Ingólfsson, O. Gas Phase Low Energy Electron Induced Decomposition of the Focused Electron Beam Induced Deposition (FEBID) Precursor Trimethyl (Methylcyclopentadienyl) Platinum(IV) (MeCpPtMe3). *Phys. Chem. Chem. Phys.* **2012**, *14*, 14611−14618.

(8) Engmann, S.; Stano, M.; Papp, P.; Brunger, M. J.; Matejčík, Š.; Ingólfsson, O. Absolute Cross Sections for Dissociative Electron Attachment and Dissociative Ionization of Cobalt Tricarbonyl Nitrosyl in the Energy Range from 0 to 140 eV. *J. Chem. Phys.* **2013**, *138*, 044305.

(9) Allan, M. Electron Scattering in $Pt(PF_3)_4$: Elastic Scattering, Vibrational, and Electronic Excitation. *J. Chem. Phys.* **2011**, *134*, 204309.

(10) Landheer, K.; Rosenberg, S. G.; Bernau, L.; Swiderek, P.; Utke, I.; Hagen, C. W.; Fairbrother, D. H. Low-Energy Electron-Induced Decomposition and Reactions of Adsorbed Tetrakis-(trifluorophosphine)platinum [Pt(PF3)4]. *J. Phys. Chem. C* **2011**, *115*, 17452−17463.

(11) te Velde, G.; Bickelhaupt, F. M.; Baerends, E. J.; Fonseca Guerra, C.; van Gisbergen, S. J. A.; Snijders, J. G.; Ziegler, T. Chemistry with ADF. *J. Comput. Chem.* **2001**, *22*, 931−967.

(12) ADF: Density Functional Theory (DFT) Software for Chemists, Version 2013.01; http://www.scm.com/, 2013.

DOI: 10.1021/acs.jpcc.6b02660
J. Phys. Chem. C 2016, 120, 10667−10674

(13) Becke, A. D. A. Multicenter Numerical Integration Scheme for Polyatomic Molecules. *J. Chem. Phys.* **1988**, *88*, 2547−2553.
(14) Franchini, M.; Philipsen, P. H. T.; Visscher, L. The Becke Fuzzy Cells Integration Scheme in the Amsterdam Density Functional Program Suite. *J. Comput. Chem.* **2013**, *34*, 1819−1827.
(15) Lenthe, E. v.; Baerends, E. J.; Snijders, J. G. Relativistic Regular Two-Component Hamiltonians. *J. Chem. Phys.* **1993**, *99*, 4597−4610.
(16) Vosko, S. H.; Wilk, L.; Nusair, M. Accurate Spin-Dependent Electron Liquid Correlation Energies for Local Spin Density Calculations: a Critical Analysis. *Can. J. Phys.* **1980**, *58*, 1200−1211.
(17) Stephens, P. J.; Devlin, F. J.; Chabalowski, C. F.; Frisch, M. J. Ab Initio Calculation of Vibrational Absorption and Circular Dichroism Spectra Using Density Functional Force Fields. *J. Phys. Chem.* **1994**, *98*, 11623−11627.
(18) Grimme, S.; Antony, J.; Ehrlich, S.; Krieg, H. A Consistent and Accurate Ab Initio Parametrization of Density Functional Dispersion Correction (DFT-D) for the 94 Elements H-Pu. *J. Chem. Phys.* **2010**, *132*, 154104.
(19) Grimme, S.; Ehrlich, S.; Goerigk, L. Effect of the Damping Function in Dispersion Corrected Density Functional Theory. *J. Comput. Chem.* **2011**, *32*, 1456−1465.
(20) Ziegler, T.; Rauk, A. On the Calculation of Bonding Energies by the Hartree Fock Slater Method. *Theor. Chim. Acta* **1977**, *46*, 1−10.
(21) Mitoraj, M. P.; Michalak, A.; Ziegler, T. A Combined Charge and Energy Decomposition Scheme for Bond Analysis. *J. Chem. Theory Comput.* **2009**, *5*, 962−975.
(22) Gritsenko, O.; Schipper, P.; Baerends, E. Approximation of the Exchange-Correlation Kohn-Sham Potential with a Statistical Average of Different Orbital Model Potentials. *Chem. Phys. Lett.* **1999**, *302*, 199−207.
(23) Gruening, M.; Gritsenko, O. V.; van Gisbergen, S. J. A.; Jan Baerends, E. On the Required Shape Corrections to the Local Density and Generalized Gradient Approximations to the Kohn-Sham Potentials for Molecular Response Calculations of (Hyper)-Polarizabilities and Excitation Energies. *J. Chem. Phys.* **2002**, *116*, 9591−9601.
(24) Koch, W.; Holthausen, M. C. *A Chemist's Guide to Density Functional Theory*; Wiley-VCH Verlag GmbH: Weinheim, 2001.
(25) Kepp, K. P. Consistent Descriptions of Metal-Ligand Bonds and Spin-Crossover in Inorganic Chemistry. *Coord. Chem. Rev.* **2013**, *257*, 196−209.
(26) Siegbahn, P. E. M.; Blomberg, M. R. A.; Chen, S.-L. Significant van der Waals Effects in Transition Metal Complexes. *J. Chem. Theory Comput.* **2010**, *6*, 2040−2044.
(27) Dreuw, A.; Weisman, J. L.; Head-Gordon, M. Long-range charge-transfer excited states in time-dependent density functional theory require non-local exchange. *J. Chem. Phys.* **2003**, *119*, 2943−2946.
(28) Grimme, S.; Hujo, W.; Kirchner, B. Performance of Dispersion-Corrected Density Functional Theory for the Interactions in Ionic Liquids. *Phys. Chem. Chem. Phys.* **2012**, *14*, 4875−4883.
(29) Drews, T.; Rusch, D.; Seidel, S.; Willemsen, S.; Seppelt, K. Systematic Reactions of $[Pt(PF_3)_4]$. *Chem. - Eur. J.* **2008**, *14*, 4280−4286.
(30) Ritz, C. L.; Bartell, L. S. Molecular Structure of $Pt(PF_3)_4$ by Gas-Phase Electron Diffraction. *J. Mol. Struct.* **1976**, *31*, 73−76.
(31) Bligh-Smith, R. M.; Edwards, H. G. M.; Fawcett, V. Force-Constant Calculations for $Ni(PF_3)_4$, $Pd(PF_3)_4$ and $Pt(PF_3)_4$. *Spectrochim. Acta, Part A* **1987**, *43*, 1069−1073.
(32) Hu, P.; Luo, Q.; shu Li, Q.; Xie, Y.; King, R. B.; Schaefer, H. F. Construction of the Tetrahedral Trifluorophosphine Platinum Cluster $Pt_4(PF_3)_8$ from Smaller Building Blocks. *Inorg. Chem.* **2014**, *53*, 5300−5310.
(33) Friedman, J. F.; Miller, T. M.; Friedman-Schaffer, J. K.; Viggiano, A. A.; Rekha, G. K.; Stevens, A. E. Electron Attachment to $Ni(PF_3)_4$ and $Pt(PF_3)_4$. *J. Chem. Phys.* **2008**, *128*, 104303.
(34) Lacko, M.; Papp, P.; Wnorowski, K.; Matejčík, Š. Electron-Induced Ionization and Dissociative Ionization of Iron Pentacarbonyl Molecules. *Eur. Phys. J. D* **2015**, *69*, 84.
(35) Sebetci, A. Does Spin-Orbit Coupling Effect Favor Planar Structures for Small Platinum Clusters? *Phys. Chem. Chem. Phys.* **2009**, *11*, 921−925.
(36) Blaise, J.; Verges, J.; Wyart, J.-F.; Engleman, R. Energy Levers of Neutral Platinum. *J. Res. Natl. Inst. Stand. Technol.* **1992**, *97*, 213−216.
(37) Fey, N.; Orpen, A. G.; Harvey, J. N. Building Ligand Knowledge Bases for Organometallic Chemistry: Computational Description of Phosphorus(III)-Donor Ligands and the Metal-Phosphorus bond. *Coord. Chem. Rev.* **2009**, *253*, 704−722.
(38) Mitoraj, M. P.; Michalak, A. σ-Donor and π-Acceptor Properties of Phosphorus Ligands: An Insight from the Natural Orbitals for Chemical Valence. *Inorg. Chem.* **2010**, *49*, 578−582.
(39) Lassettre, E. N.; Francis, S. A. Inelastic Scattering of 390-V Electrons by Helium, Hydrogen, Methane, Ethane, Cyclohexane, Ethylene, and Water. *J. Chem. Phys.* **1964**, *40*, 1208.
(40) Abedin-Siddique, Z.; Ohno, T.; Nozaki, K.; Tsubomura, T. Intense Fluorescence of Metal-to-Ligand Charge Transfer in [Pt(0)(binap)2] [binap = 2,2′-Bis(diphenylphosphino)-1,1′-binaphthyl]. *Inorg. Chem.* **2004**, *43*, 663−673.
(41) Haneder, S.; Da Como, E.; Feldmann, J.; Lupton, J. M.; Lennartz, C.; Erk, P.; Fuchs, E.; Molt, O.; Munster, I.; Schildknecht, C.; et al. Controlling the Radiative Rate of Deep-Blue Electrophosphorescent Organometallic Complexes by Singlet-Triplet Gap Engineering. *Adv. Mater.* **2008**, *20*, 3325−3330.
(42) Koehler, A.; Baessler, H. Triplet States in Organic Semiconductors. *Mater. Sci. Eng., R* **2009**, *66*, 71−109.
(43) Griffith, J. S. *The Theory of Transition-Metal Ions*, 2nd ed.; Cambridge University Press: 1964.
(44) Siddique, Z. A.; Yamamoto, Y.; Ohno, T.; Nozaki, K. Structure-Dependent Photophysical Properties of Singlet and Triplet Metal-to-Ligand Charge Transfer States in Copper(I) Bis(diimine) Compounds. *Inorg. Chem.* **2003**, *42*, 6366−6378.
(45) Bakova, R.; Chergui, M.; Daniel, C.; V, A., Jr.; Zalis, S. Relativistic Effects in Spectroscopy and Photophysics of Heavy-Metal Complexes Illustrated by Spin-Orbit Calculations of $[Re(imidazole)(CO)_3(phen)]^+$. *Coord. Chem. Rev.* **2011**, *255*, 975−989.
(46) Bersuker, I. B. *The Jahn-Teller Effect*; Cambridge University Press: 2006.
(47) Schaefer, J.; Hoelzl, J. A Contribution to the Dependence of Secondary Electron Emission from the Work Function and Fermi Energy. *Thin Solid Films* **1972**, *13*, 81−86.
(48) Steinmann, W. Spectroscopy of Image-Potential States by Two-Electron Emission. *Appl. Phys. A: Solids Surf.* **1989**, *49*, 365−377.
(49) Fauster, T. Quantization of Electronic States on Metal Surfaces. *Appl. Phys. A: Solids Surf.* **1994**, *59*, 479−486.
(50) Fowlkes, J. D.; Randolph, S. J.; Rack, P. D. Growth and Simulation of High-Aspect Ratio Nanopillars by Primary and Secondary Electron-Induced Deposition. *J. Vac. Sci. Technol., B: Microelectron. Process. Phenom.* **2005**, *23*, 2825.
(51) Kunz, R. R.; Allen, T. E.; Mayer, T. M. Selective Area Deposition of Metals Using Low-Energy Electron Beams. *J. Vac. Sci. Technol., B: Microelectron. Process. Phenom.* **1987**, *5*, 1427−1431.

DOI: 10.1021/acs.jpcc.6b02660
J. Phys. Chem. C 2016, 120, 10667−10674